# RIVULET DYNAMICS
# WITH VARIABLE GRAVITY AND WIND SHEAR

FINAL REPORT

Prepared by

Jeffrey S. Marshall and Robert Ettema

Submitted to

NASA Office of Biological and Physical Research
98 NRA Grant NAG3-2368
Dr. Charles Neiderhaus, Project Manager


IIHR Technical Report No. 440

IIHR – Hydroscience & Engineering
College of Engineering
The University of Iowa
Iowa City, IA 52242-1585 USA

November 2004

## Summary

The project involved examination of the effect of gravity and wind shear on the formation, dynamics, and breakup of liquid rivulets under a variety of different gravitational states, ranging from terrestrial gravity to microgravity. Secondary variables found to be important to understanding the project results include liquid film inertia (as typified by the film Reynolds number) and surface contamination (as typified by variation in contact angle). Surface contamination was found to play a particularly important role for low Reynolds number flows. The microgravity experimental conditions conducted on-board the KC-135 were of limited time span (less than about 25 seconds each), so we consequently focused the experimental work on problems with higher Reynolds number flows in order to complete the experimental run in the given time period. The computational method that we used, on the other hand, assumes small or moderate Reynolds number. We are currently working on extending the Reynolds number range of this method, as well as implementing an entirely new computational method that is suitable to arbitrary Reynolds number flows.

Major results obtained in the high- and low-Reynolds number regime investigations are summarized below, followed by listings of students supported by the project and papers and theses published under project support. The high-Reynolds number experiments and related analysis found that wind-driven rivulet and surface-attached droplet flows are dramatically different when comparing microgravity and terrestrial gravity states, as well as when comparing wind-driven films to films driven by gravity or centrifugal force under any given gravitational state. These findings are in contrast to the prevailing assumptions in the liquid-film literature (based mainly on experience with low-Reynolds number films) that liquid films are fairly gravity-independent and that shear-driven and gravity-driven films behave in much the same way.

The principal observations from our high-Reynolds number experimental investigation include: (1) for all the levels of wind shear and liquid flow rates examined, rivulets broke up to form small droplets (whereas the gravity-driven rivulets exhibited broad regimes

with no breakup); (2) the rivulet break-off frequency was measured to be an order of magnitude larger for microgravity than for terrestrial gravity conditions, under similar flow conditions; (3) droplets in microgravity at times exhibited an interesting "inch-worming" motion, for which there is no comparable droplet motion in terrestrial gravity; (4) in terrestrial gravity, the droplets exhibited two distinct lateral lobes, leading to bifurcation of the droplets into multiple "offspring" droplets (no similar bifurcation phenomena was observed for gravity-driven flow or in microgravity). An approximate analysis was introduced which allowed us to develop correlations collapsing our data for many of the measured quantities. Work is on-going to extend our experimental investigations and develop computational models for the droplet bifurcation phenomenon observed in terrestrial gravity.

Our low-Reynolds number computational investigation focused on examining the effect of surface contamination on the rivulet development through the fingering instability, as well as on the effect of normal gravity on inhibiting the fingering instability and smoothing out the film thickness variation introduced by surface contamination. Within the context of the lubrication approximation (applicable to low Reynolds number and small film slopes), there is not much qualitative difference between shear-driven and gravity-driven film flows.

The principal findings of our low Reynolds number investigation include: (1) the precursor film method for resolving the moving contact angle singularity can be extended to account for variation in static contact angle by addition of a "disjoining pressure" on the film top interface, and the predictions of the extended formulation are observed to satisfy the Tanner-Hoffman-Voinov dynamic contact angle formula for sufficiently small values of the precursor film thickness; (2) the fingering wavelength for driven liquid film flow through an array of contamination "spots" locks on to the spacing distance between the spots until the spot separation distance becomes less than a critical value, which is less than the critical wavelength for fingering instability; (3) surface contamination can generate sub-critical instabilities, in which fingering of the film front occurs even under conditions for which the film is stable to linear theory; (4) normal body force

significantly suppresses the effect of surface contamination on perturbing and inducing instability of the driven liquid front. Work is on-going to examine film fingering on surfaces with random variation of static contact angle, which are typified by a correlation length and a variance.

## Rivulet Dynamics with Variable Gravity and Wind Shear

# RIVULET DYNAMICS WITH VARIABLE GRAVITY AND WIND SHEAR

## I. High-Reynolds Number Investigation: Wind-Driven Rivulet Breakup and Surface-Attached Droplet Flows

The ensuing sections describe rivulet formation for a range of gravity situations: 1*g*, 0*g*, and intermediate values of gravity acceleration. Applications involving rivulet flow where 0*g* and partial-*g* values pertain include rivulets on aircraft with sharply curved trajectories and various mechanical coating and cooling processes used during space flight on potential future lunar and Martian space stations.

### A. Experimental Description

Experiments were conducted in the open-loop "rivulet wind-tunnel", shown in Figure 1. The bottom surface of the rivulet wind-tunnel consists of a flat Plexiglas sheet measuring 0.3 m wide and 1 m long. The top surface of the rivulet wind-tunnel is another Plexiglas sheet mounted parallel to and at a distance of 0.05 m above the bottom surface. Air flow through these two surfaces was generated by a blower placed upstream of the channel formed by the Plexiglas plates. A honeycomb is placed inside the blower to help make the exit flow uniform. The maximum velocity that can be produced by the blower in the wind-tunnel is 13 m/s. Wind speed was measured at different points over the width of the wind-tunnel exit using a Pitot tube and Rouse manometer. Distilled water, used as the working fluid, is pumped to the test surface using a positive-displacement pump. The liquid reservoir sides are flexible so as to allow the reservoir to collapse and avoid air or cavitation bubbles as the water is pumped out of the reservoir, which is desirable in the microgravity experiments. Liquid flow rate is controlled using a precision needle valve. The liquid is injected into the test section through a 2 mm hole centered on the upstream end of the bottom Plexiglas surface of the rivulet wind-tunnel. At the end of the test section, the liquid is collected in a trap through a slot in the bottom of the test surface, which is filled with a highly absorbent cloth material to capture the water. As additional measures to prevent liquid from escaping into the surroundings, a honeycomb is added at the end of the test section and a deflector shield is placed downwind of the honeycomb. The inner side of the deflector shield is covered with absorbent cloth to catch any remaining water droplets.

The microgravity experiments (zero- and partial-gravity) were conducted on four flights of the KC-135 aircraft, with about 40 parabolas per flight. Each parabola provided about 15 seconds of usable microgravity conditions for testing. The test conditions were selected to provide data on as many different flow regimes as possible, and tests with each combination of wind and liquid flow conditions was repeated between three to five times in order to ensure repeatable data. The water flow was turned off between each parabola, but the air flow was left on in order to dry out the test section and clear it of residual water. The flow was filmed using digital video both from above the test section and from the side of the test section. The experimental procedure used for the terrestrial gravity experiments was similar to that described above, with the difference that the experiment was allowed to run for a much longer period.

Relative gravity data, obtained using an accelerometer, were provided by NASA. Although most tests were conducted for zero-gravity conditions, some tests were also performed for partial gravity states, including 0.16g, 0.25g, and 0.38g. The 0.16g and 0.38g conditions correspond to the gravitational force on the Moon and on Mars, respectively.

The wind speed was varied between about 7 - 12 m/s, and the width of the enlarged rivulet "head" (or the subsequent droplet after head detachment) varied between about 4 - 12 mm. Choosing nominal values for wind speed and droplet width of $U = 10$ m/s and $d = 8$ mm, respectively, the aerodynamic Reynolds number is $\mathrm{Re} = Ud/\nu_{air} = 5300$, the Weber number is $We = \rho_{air} U^2 d/\sigma = 13$, and the Bond number (in 1g) is $Bo = \rho_{water} g d^2/\sigma = 8.6$. For Weber and Bond numbers in this range we would expect the inertial deformation and gravitational flattening of the rivulet head and droplets to both be significant.

This flow exhibited a natural variability associated with the effect of contact angle hysteresis on the rivulet and droplet conditions. The uncertainty due to this natural flow variability is in nearly all cases larger than the measurement uncertainty. Details of the data uncertainty in 1g are given in the next section, which describes the specific data

measured. A comprehensive uncertainty analysis was more difficult to perform for the microgravity experiments conducted on the NASA KC-135 parabolic-flight aircraft due to the limited number and short duration of the tests, particularly for the partial gravity conditions. Checks on the performance of the experimental apparatus indicate that similar accuracies of control and measurement existed for the microgravity conditions as for the terrestrial-gravity conditions. The uncertainty in averages reported for aspects of the flow exhibiting natural variability were higher in microgravity than in 1g, however, due to the necessity of having fewer test results over which to average the data.

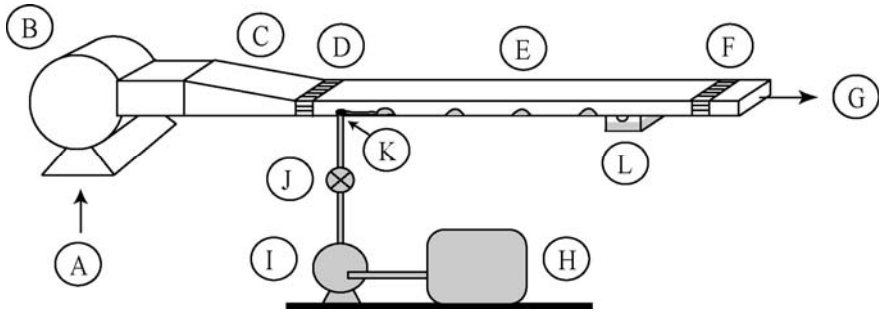


Figure 1. Sketch of the rivulet wind tunnel showing (A) air inlet, (B) blower, (C) contraction, (D) honeycomb, (E) test section, (F) honeycomb water trap, (G) air outlet, (H) collapsible water storage tank, (I) positive-displacement pump, (J) needle valve, (K) water inlet hole, (L) water collection box.

B. Terrestrial Gravity Results

We start with a fixed non-zero liquid and gradually increase the wind speed. For a wind speed of 0 m/s, there will be no rivulet, and a circular puddle will spread laterally from the inlet due to hydrostatic pressure until colliding with sides of the test section. As the wind speed is increased, a puddle still spreads from the inlet. However, the puddle's shape is increasingly distorted from a circle to an ellipse that is shifted downstream of the inlet. Additionally, the puddle becomes wavy and oscillates irregularly. For higher wind speeds, the puddle is shifted completely downstream of the inlet. When this occurs, water spreads as an unusual fan-shaped puddle extending from the water source (Figure 2b). The apex angle of the fan decreases as wind speed increases.

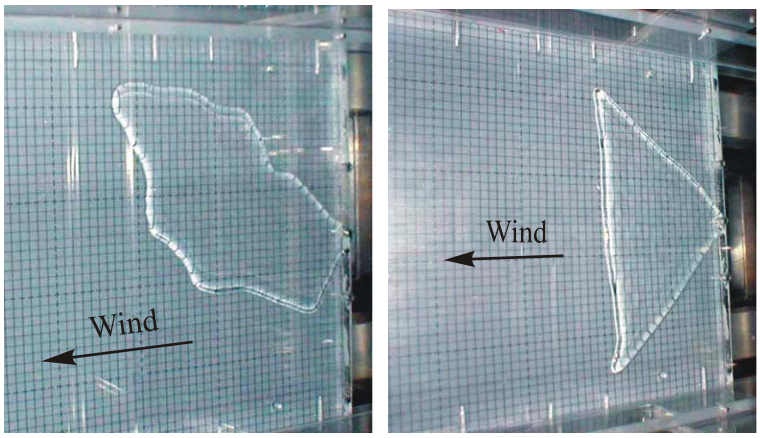


(a) (b)

Figure 2. (a) At very low wind speeds, a puddle of water forms around the water outlet and spreads downwind; (b) increasing wind speed causes the puddle to become fan-shaped. The surface is horizontal in both cases.

For higher wind speeds, a rivulet forms from the water ejected from the hole, which is initially straight with a nearly uniform width but with a somewhat thicker and wider "head" at the downstream end (Figure 3a). After the rivulet progresses a short distance, the forward progression of this head is observed to stop and grow to form a large droplet (Figure 3b), fed by the rivulet, that continues to increase in size with time. This large droplet spreads laterally as it increases in volume, forming a raised ridge just behind the downstream contact line, which is subject to significant form drag. The aerodynamic drag on the droplet increases with time as its volume grows until a critical point is reached at which the downstream aerodynamic force balances the upstream surface-tension force. At this point the droplet breaks off the rivulet and advects downstream, and the cycle repeats itself.

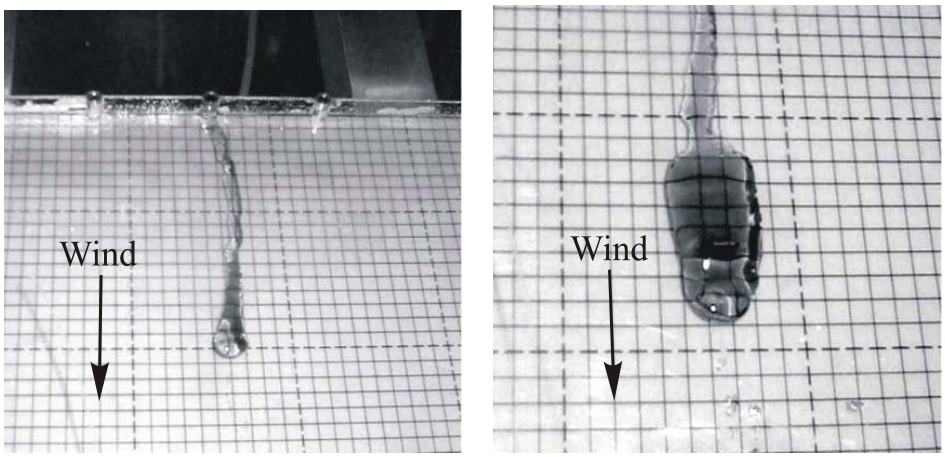


(a) (b)

Figure 3. Photographs showing break-up of a wind-driven rivulet to form a droplet in 1*g*, including (a) the rivulet at a time where it has stopped progressing and is beginning to form a large droplet, and (b) close-up of the droplet about to detach from the rivulet. Wind flow is from top to bottom.

The break-off of the droplet at the end of the rivulet is resisted by surface-tension forces acting at the contact lines. The surface-tension force arises from the difference in contact angle between the front and the back of a droplet, typically called the advancing and receding angles, respectively. As the aerodynamic drag (or gravitational force for rivulets on a slope) attempting to drive the stationary droplet forward is increased, the receding and advancing contact angles approach their limiting values at zero velocity. The surface-tension force thus has a maximum value that occurs when the two contact angles have reached their limiting values, and if the driving aerodynamic or gravitational force exceeds this maximum value the droplet will begin moving forward. This condition for forward motion of a droplet is essentially the same as that for break-off of the droplet from the end of the rivulet, and can thus be used to determine the critical volume of the droplet and hence the rivulet break-off frequency. A criterion for rivulet break-off period $T$ was developed based on this argument of the form (McAlister, Ettema & Marshall, 2004)

$$T = \frac{2\pi}{3Q}\left(\frac{8\sigma}{\pi\rho U^2 C_D}\right)^3 C, \qquad (1)$$

where Q is the water flow rate, U is the air speed, ρ is the liquid density, σ is the interface surface tension, $C_D$ is the droplet aerodynamic drag coefficient, and $C$ is a constant that depends on the advancing and receding contact angles. A set of numerical computations were performed using a finite-volume code (see section 1.4.) that give a value of about 0.6 for $C_D$. This prediction is found to collapse all of our experimental data for rivulet break-off period, as shown in Figure 4.

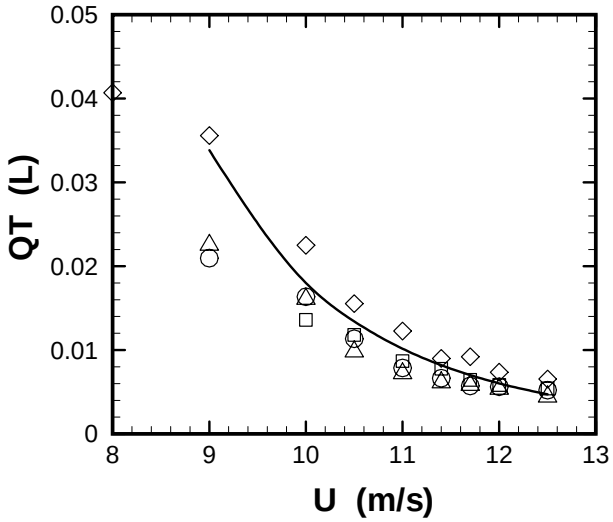


Figure 4. Data for (a) rivulet break-off period $T$ and (b) product of rivulet break-off period $T$ and the water flow rate $Q$ versus air speed $U$ for the terrestrial gravity (1g) case, for values of water flow rate of $Q = 10$ mL/min (squares), 15 mL/min (deltas), 20 mL/min (circles), and 40 mL/min (diamonds). The solid line is the theoretical prediction given by Eqn. (1) with $C = 0.5$.

When the droplet detaches and progresses downstream under the influence of the wind drag, it quickly reshapes itself in accordance with the airflow pressure distribution, the surface-tension and bottom-shear forces. The droplet evolves into an elongated, double-lobed shape as shown in Figure 5b. The elongation of the droplets is in the cross-stream (rather than streamwise) direction, and occurs in response to the low pressure at the droplet sides. Figure 5 shows several examples of downstream-propagating droplets on a flat surface. The liquid layer is significantly thicker within the lobes at the ends of the elongated droplet than at the center. Droplets are observed to gradually spread in the

lateral direction, attaining progressively greater aspect ratio until they suddenly bifurcate into two droplets. These offspring droplets themselves subsequently elongate laterally as they continue their downstream progression, although at a smaller speed than the original parent droplet. Since in general larger droplets travel faster than slower droplets, there exists sufficiently far downstream a large diversity of droplet sizes and speeds. This situation gives rise to the occurrence of droplet collisions, in which a larger droplet will overtake and collide with a smaller droplet. Droplets coalesce upon collision forming a single larger droplet that continues moving downstream at a yet more rapid speed. This larger droplet gradually elongates and bifurcates, repeating the cycle. The resulting droplet flow sufficiently far downstream of the rivulet injection point is dominated by series of droplet collision, elongation and bifurcation events that appear to occur in a random manner. Plots showing a collection of data on average number of bifurcations and collisions as the droplet travels over the test section are shown in Figure 6. These bifurcations and collisions seem to peak between air flow velocities of about 10 and 12 m/s, corresponding to the range of air flow rates for which development of roller droplets is most prominent.

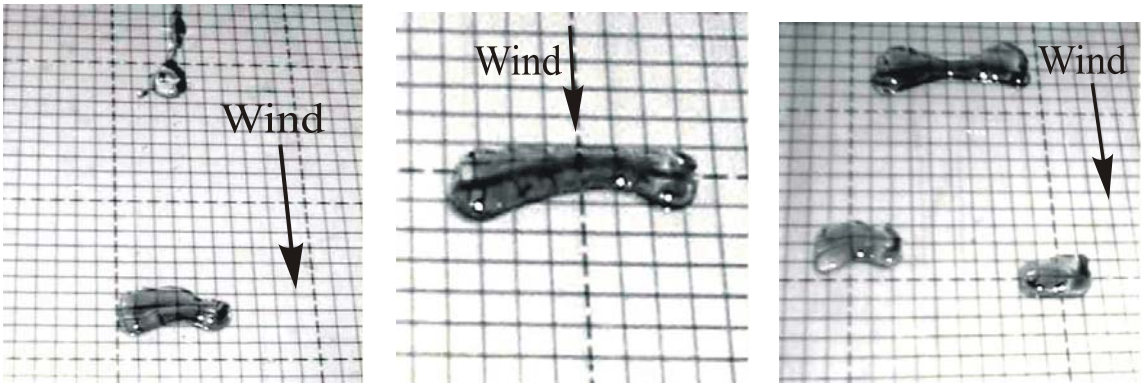


(a) (b) (c)

Figure 5. Examples of downstream-propagating droplets on a horizontal surface in 1*g*: (a) droplet shortly after break-off from rivulet, (b) close-up view of the elongated, double-lobe structure of the droplet, and (c) a larger droplet overtaking two smaller droplets. Wind flow is from top to bottom.

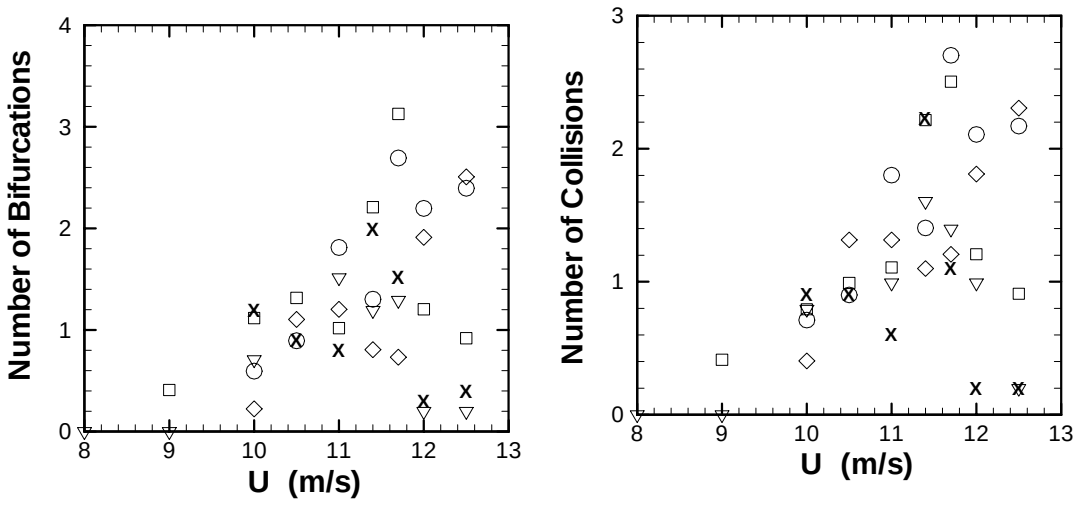


(a) (b)

Figure 6. Graphs of droplet bifurcations and collisions for the terrestrial gravity experiments, showing average number of times a single droplet (a) bifurcates and (b) collides with another droplet as it traverses the test surface for cases with water flow rate $Q = 5$ mL/min (crosses), 10 mL/min (squares), 15 mL/min (deltas), 20 mL/min (circles), and 40 mL/min (diamonds).

C. Microgravity Results

Our experiments on rivulets in micro-gravity conditions reveal very significant differences between wind-driven rivulets under different gravitational states, as well as between gravity-driven and wind-driven rivulets in general. The micro-gravity conditions examined include 0*g* as well as Martian and Lunar gravities (0.16*g* and 0.38*g*, respectively). The experiments were carried out on NASA's KC-135 aircraft.

In the zero-gravity experiments, the absence of gravitational force allowed the rivulet head shape to be set primarily by surface tension, which leads to a nearly hemispherical shape (Figure 7). This difference in rivulet head shape significantly increased form-drag on the microgravity rivulet, in comparison to a terrestrial gravity case with the same air and water flow rates, which profoundly altered the subsequent flow behavior. When the aerodynamic drag on the rivulet head becomes sufficiently large, the head detaches from the rivulet to form a droplet, which propagates downstream with nearly hemispherical shape and with nearly constant speed. Droplets did not bifurcate in the zero-gravity

experiments, and all droplets observed in a given experiment have fairly uniform size and velocity. The absence of strong velocity differences makes the occurrence of droplet collisions for the microgravity cases very rare.

One of the most prominent differences between the zero-gravity and terrestrial gravity experiments is that the rivulet break-off frequency is nearly an order of magnitude greater in zero-gravity than it is for the same air and water flow rates in terrestrial gravity. The increase in break-off frequency for the zero-gravity experiments is due to the increased form-drag experienced by the rivulet head due to its elevated shape. The prediction from the scaling in Eqn. (1) is indicated by the three curves in Figure 8, corresponding to air speeds of $U = 10\,\text{m/s}$, 11 m/s, and 12 m/s, from bottom to top in the figure. These predictions are obtained using a value of 0.05 for the coefficient *C* in (1), which is an order of magnitude smaller than the value of the coefficient in the 1g experiments. The difference in value of *C* results from the fact that the rivulet head is more nearly hemispherical for the microgravity experiments. The experimental data exhibit much greater scatter than for the 1g experiments, likely due to the noisy environment on-board the KC-135 and the greater uncertainty consequent to fewer experimental repetitions.

A plot of the maximum height of the rivulet head at the break-off point is given in Figure 9 as a function of air flow speed. As expected, the critical height at break-off decreases with increase in air speed and is approximately independent of water flow rate. A theoretical prediction of the maximum height is developed by McAlister, Ettema and Marshall (2004) as

$$h_{crit} = \frac{8\sigma}{\pi \rho U^2 C_D} A, \qquad (2)$$

where A is an adjustable constant. The scaling estimate $h_{crit} = const \times U^{-2}$ is plotted in Figure 9, with the empirical constant chosen as $A = 3.7$. This prediction falls within the data scatter, although the best-fit curve to the data seems to vary more sensitively with air speed *U*.

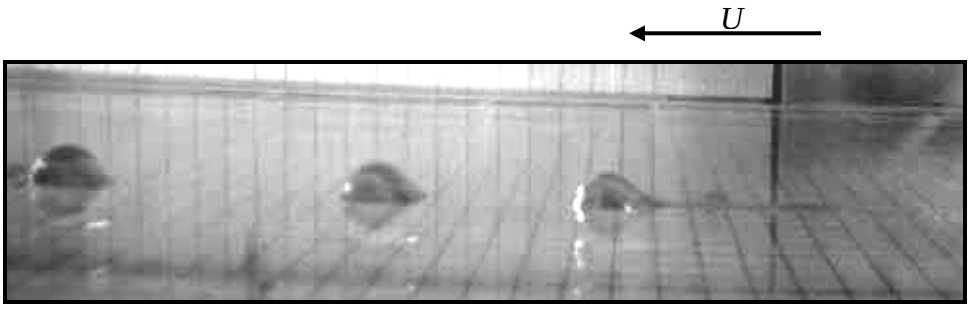


Figure 7. Periodic shedding showing two nearly hemispherical droplets with a third about to break off from the end of the rivulet for zero-gravity case ($Q$ = 15 mL/min, $U$ = 11.8 m/s). The grid lines have a spacing of 6 mm.

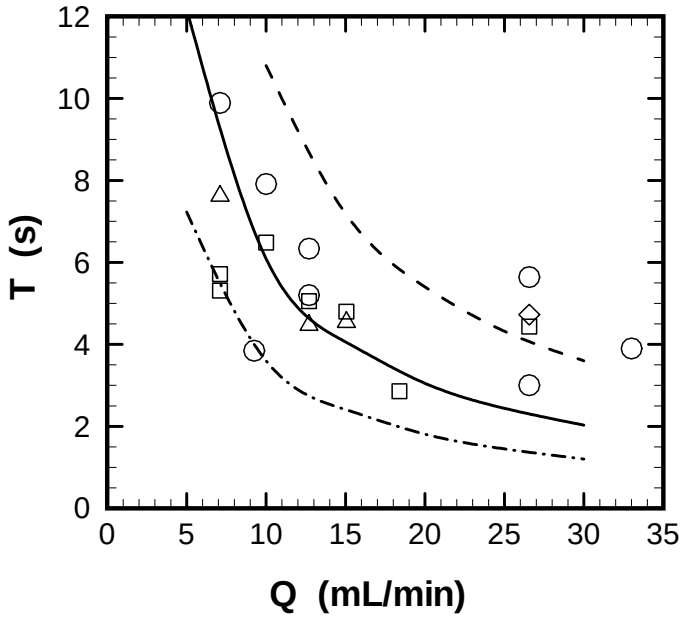


Figure 8. Period of rivulet break-off in zero-gravity versus the water discharge rate, for cases with $Q = 10.3$ mL/min (squares), 11.4 mL/min (deltas), 11.9 mL/min (circles), and 12.5 mL/min (diamonds). The curves give the theoretical predictions from Eqn. (1) with $C = 0.05$ for $U = 10$ m/s (dashed), 11 m/s (solid) and 12 m/s (dashed-dotted).

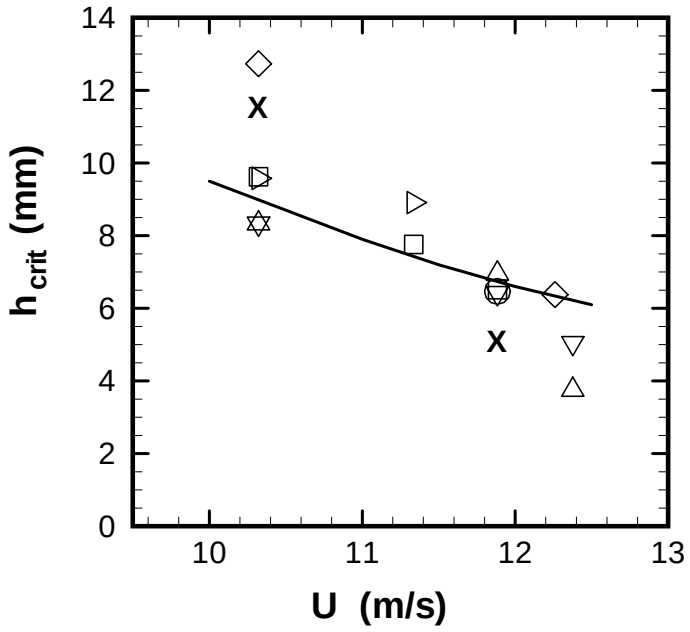


Figure 9. The average height of the rivulet head at the break-off time for all zero-gravity experiments, where $Q = 7$ mL/min (squares), 10 mL/min (deltas), 12.5 mL/min (gradients), 18.5 mL/min (right triangles), 26.5 mL/min (crosses), 33 mL/min (circles). The curve represents the theoretical prediction from Eq. (2) with $A = 3.7$.

Sometimes as the droplet progressed downstream, a tail of fluid formed behind the droplet's trailing edge. This tail occurred with high wind speed, and was quite stable and did not separate from the droplet. An interesting phenomenon involving this droplet tail arose when the droplet momentarily stalled on the test surface, which we refer to as "inchworm motion" due to its similarity with the motion of an inchworm. The various steps of the inchworm phenomenon are illustrated in Figure 10, which first shows a droplet with a tail propagating on the substrate surface. The onset of the inchworm motion is typified by elongation and flattening of the front lobe of the droplet. Transport of water from the flattened front lobe into the tail section leads to formation of a large rear lobe preceded by a small front lobe at the half-cycle point. The water from the tail then suddenly sloshes back to the front lobe and the droplet simultaneously lurches forward. The inchworm motion was found to be more prevalent for higher wind speeds, above 11 m/s, and the inchworm cycle repeated several times before the droplet returned to a steadily propagating state. The period of oscillation for the inchworm oscillation

varied between 0.6 sec and 1 sec, and appeared not to be particularly sensitive to the air or water flow rates.

| Plan View | Side View | Comments |
|---|---|---|
| 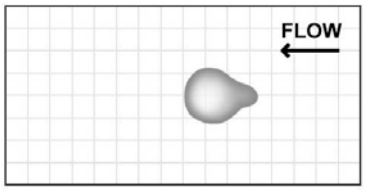  |   | Typical zero-gravity droplet with small tail. |
| 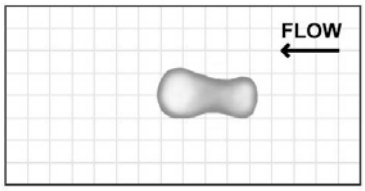  |   | The aerodynamic load on the main lobe the droplet pulls it along faster than the tail can move, creating a thin section in the middle. |
| 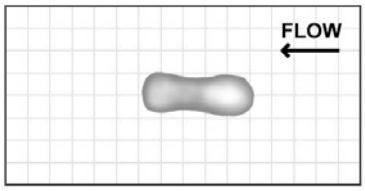  |   | Water within droplet sloshes toward tail and droplet becomes flattened. |
| 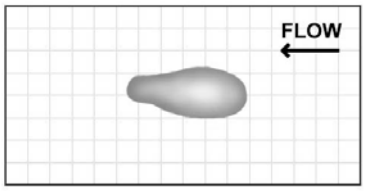  |   | Droplet forms a nearly hemispherical shape, but with most of the water in the upstream “tail” portion. |
| 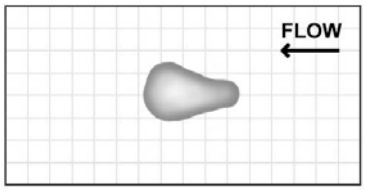  |   | Water sloshes back to downstream lobe, and droplet simultaneously lurches forward. The process then repeats. |

Figure 10. Typical sequence illustrating the inchworm phenomenon for zero-gravity droplet flows.

D. Partial-gravity Results

Tests were performed with several different partial-gravity states, with 0.16g (lunar gravity), 0.25g, and 0.38g (Martian gravity), and for one controlled high-gravity maneuver with 1.5g. The rivulet behavior at partial gravity exhibits aspects of that noted

above for both 0g and 1g. Photographs showing the rivulet and droplet from the side view for 0.38g and 1.5g are given in Figure 11. For 0.38g, the droplets were similar to those observed for 0g (see Figure 14), with the difference that the droplets and rivulet head are noticeably flattened. However, for the 1.5g case, with nearly the same liquid and air flow rates, the water flattened out on the substrate surface. The more streamlined, flattened shape of the rivulet head at 1.5g exhibited reduced aerodynamic drag compared to the microgravity case, and the head was not observed to break off during the period (lasting about 5 seconds) over which this enhanced gravitational state was maintained.

The rivulet break-off period is plotted for several partial-gravity conditions in Figure 12 as a function of water flow rate, with the air velocity maintained at 11 m/s. The shape of the curve is similar for all cases, but the break-off period exhibits significant increase as the gravity is increased from 0g to 0.38g. The curves in Figure 12 represent predictions of (6) using values for the coefficient $C$ of 0.05, 0.07, 0.09, and 0.11. The partial gravity data exhibit significant scatter about these curves due, at least in part, to the reduced gravity experimental conditions.

The dynamics of the detached droplets over this range of partial-gravity conditions is similar to that observed for the microgravity state. Droplet elongation in the lateral direction, or formation of roller droplets, was not observed. Nor were the droplets observed to bifurcate or collide with one another. As in the zero-gravity tests, the droplets in these partial gravity states have a fairly uniform size and velocity in any given condition.

(a)

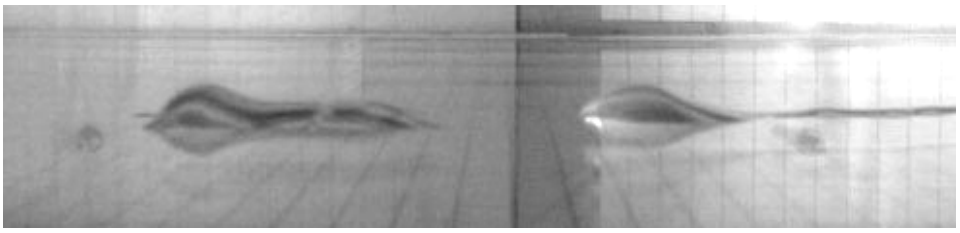

(b)

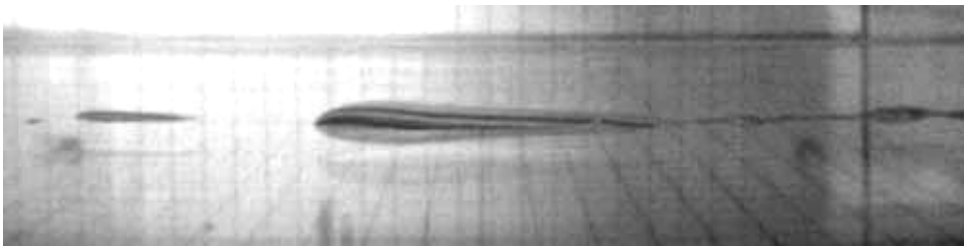

Figure 11. Photographs of the rivulet head and detached droplets for (a) 0.38g ($Q$ = 10 mL/min, $U$ = 11 m/s) and (b) 1.5g ($Q$ = 10 mL/min, $U$ = 12.4 m/s).

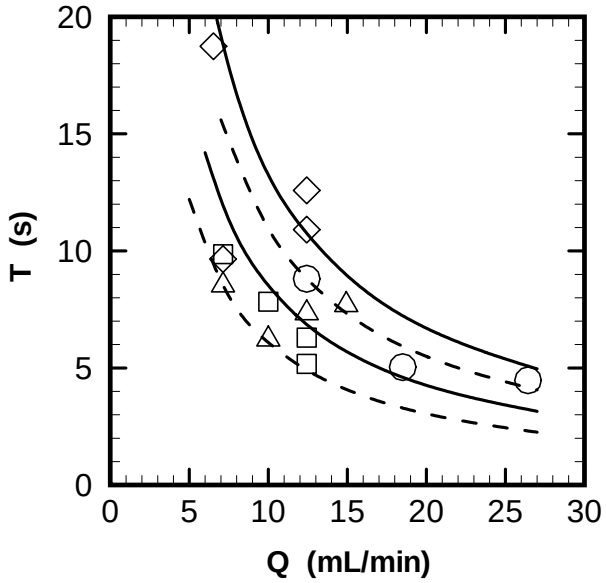


Figure 12. Period of rivulet break-off for partial-gravity cases as a function of water flowrate with air speed held constant at 11 m/s, for cases with 0 g (squares), 0.16 g (deltas), 0.26 g (circles), and 0.38 g (diamonds). Curves are predictions from Eqn. (1) with $C = 0.05$ (lower dashed), 0.07 (lower solid), 0.09 (upper dashed), and 0.11 (upper solid), respectively.

E. Flow Past Hemi-spheres and Hemi-ellipsoids

We have observed that detached droplets in microgravity conditions have a nearly hemispherical shape, whereas in terrestrial gravity conditions the droplets have a roughly hemi-ellipsoidal shape, with elongation in the cross-stream direction. Estimates of the aerodynamic drag on the droplet under these two conditions are approximated by computing air flow past fixed hemispheres and hemi-ellipsoids of various aspect ratios. The liquid velocity in the droplets is much smaller than the free-stream air velocity, and so it is neglected in estimating the aerodynamic drag.

Computations were performed using a finite-volume method (Lai, 2000) with a block-structured mesh formed of hexahedral elements. The grid points are clustered to achieve high resolution within the boundary layer both along the substrate surface and the surface of the hemi-ellipsoid, as shown in Figure 13. The numerical method stores all dependent variables at the cell centers, and it uses a novel interpolation method to yield second-order accurate approximation of the diffusive and convective fluxes on the cell boundaries for arbitrary meshes (even for unstructured meshes). The PISO algorithm is used to couple the momentum and continuity equations. In order to provide additional numerical stability, the time derivative is weighted between a second-order time derivative approximation and a first-order upwind approximation, with characteristically about 90-10 weighting ratio. The boundary conditions employed an upstream boundary layer thickness equal to 10% of the maximum height of the hemi-ellipsoid. Drag and lift coefficients are assessed by integrating the pressure and shear forces over the surface of the hemi-ellipsoid. Computations were also performed using a two-dimensional version of this code in order to examine the limit of very high ellipsoid aspect ratio.

Typical results for the pressure and shear stress magnitude on the surface of a hemisphere attached to the substrate are shown in Figure 14 for a case with $\mathrm{Re} = Ud/\nu = 6000$, where $d$ is the sphere diameter, which is representative of the droplets in our microgravity experiments. It is interesting that the high pressure in the front of the hemisphere and the low pressure in the rear of the hemisphere in Figure 14a have corresponding regions of high and low pressure, respectively, on the nearby substrate surface. Similarly, the high

shear stress magnitude on the front of the hemisphere and the low shear stress at the rear of the hemisphere in Figure 14b have corresponding region on the substrate surface.

The drag and lift coefficients for a hemisphere are plotted as a function of Reynolds number in Figure 15. For $\mathrm{Re} > 2000$, the drag coefficient asymptotes to a value of about 0.6. A plot of drag coefficient at a Reynolds number of 6000 versus aspect ratio $A \equiv b/d$ of a hemi-ellipsoid is given in Figure 16. The drag coefficient gradually increases and appears to be approaching the drag coefficient for flow past a two-dimensional hemi-circle at the same Reynolds number at large aspect ratio.

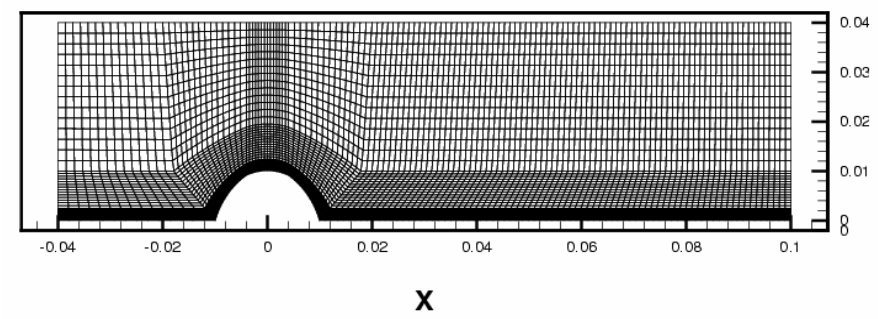


Figure 13. Section view of three-layer uniform grid at y = 0 used for simulation of air flow over a hemisphere.

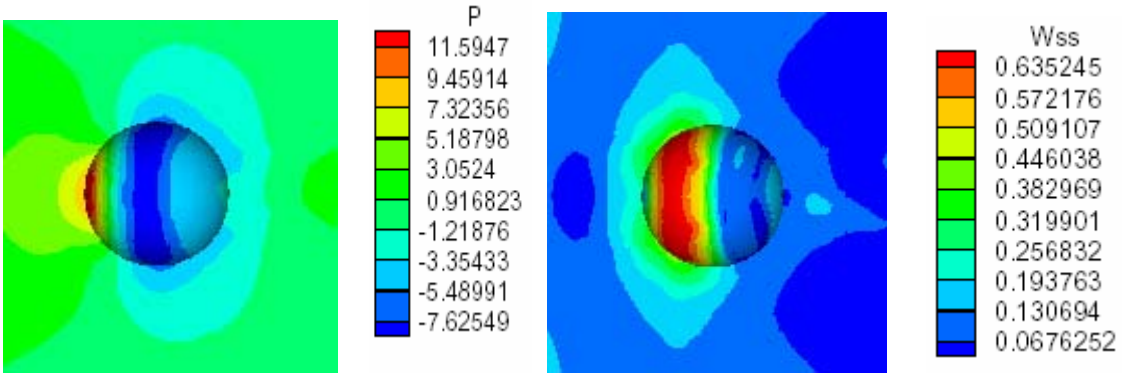


(a) (b)

Figure 14. Distribution of (a) pressure and (b) shear stress on a hemisphere attached to a flat surface with Re = 6000. Flow is from left to right.

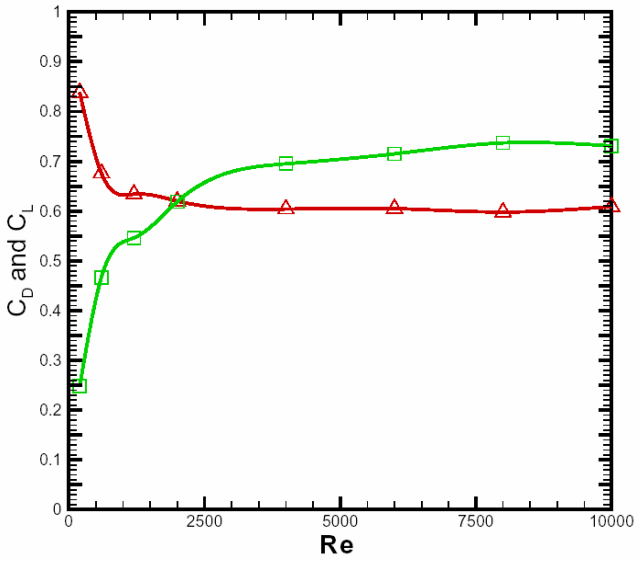


Figure 15. Variation of drag coefficient (triangles) and lift coefficient (squares) with Reynolds number for a hemisphere attached to a flat surface.

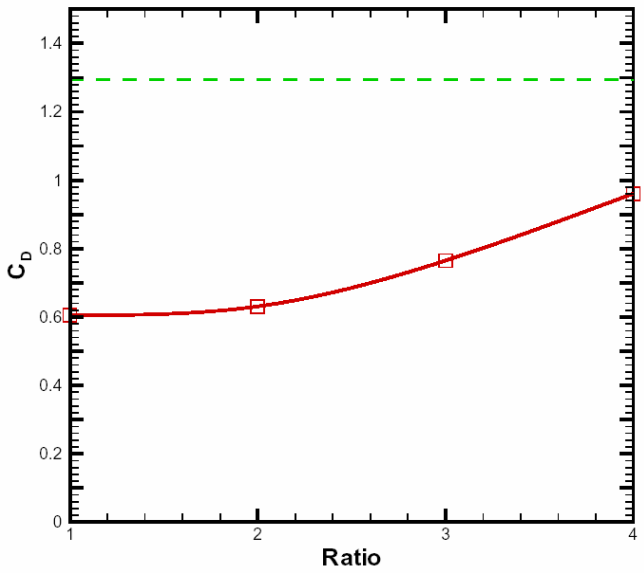


Figure 16. Variation of drag coefficient of a hemi-ellipsoid with aspect ratio for Re = 6000 . Limiting two-dimensional case is indicated by a dashed line.

## II. Low Reynolds Number Investigation: Driven Liquid Film Dynamics on Contaminated Surfaces

This section examines liquid film instability, finger growth, and subsequent rivulet development for low Reynolds number, with particular focus on the effects of gravity oriented normal to the substrate and to effects of inhomogeneity of the substrate surface, as might be caused by a dried chemical film on the surface or microscopic variation of the surface roughness. The time scale for the fingering and rivulet development in these problems is on the order of tens of minutes, which is far too long to be accommodated by the microgravity experimental apparatus available to us. For this reason, the investigation primary utilized a computational approach, based on lubrication theory. Within this low-Reynolds number regime, there are not substantial qualitative differences between flows driven by shear stresses and those driven by a body force (e.g., gravity) oriented tangent to the substrate surface. Most of the results presented in this section are for gravity-driven flows, since there are more experimental data available in the literature for gravity-driven liquid film flows.

### A. Theory and Computational Method

Integration of the Stokes equation over the width of a liquid layer with thickness $h(\mathbf{x},t)$ and use of the long-wave assumption of the standard lubrication theory yields an expression for the flow rate vector **Q** within the liquid layer tangent to the substrate surface in the presence of both normal and tangential body force components, $g_N$ and $g_T$, as

$$\mathbf{Q} = -\frac{h^3}{3\mu}[\nabla\hat{p} - \rho g_T \mathbf{e}_x + \rho g_N \nabla h], \qquad (2)$$

where $\hat{p}$ is the liquid pressure at the top surface of the layer, $\rho$ and $\mu$ are the liquid density and viscosity, respectively, $\mathbf{e}_x$ is the base vector in the direction of front motion along the plate, and $h(x,y,t)$ is the layer thickness. Substitution of (2) into the depth-

integrated continuity equation $\partial h/\partial t = -\nabla \cdot \mathbf{Q}$ yields the governing equation for liquid layer thickness as

$$\frac{\partial h}{\partial t} = \nabla \cdot \left\{ \frac{h^3}{3\mu} \left[ \nabla(\hat{p} + \rho g_N h) - \rho g_T \mathbf{e}_x \right] \right\}. \tag{3}$$

The liquid upper surface pressure can be written as a sum of a capillary pressure and an additional *disjoining pressure* term, $-\Pi$, as

$$\hat{p} = -\sigma \nabla^2 h - \Pi, \tag{4}$$

where $\sigma$ is the surface tension. An expression for $\Pi$ is given in terms of the ratio of liquid layer thickness to the constant thickness $h^*$ of the precursor film by

$$\Pi = B\left[ \left( \frac{h^*}{h} \right)^n - \left( \frac{h^*}{h} \right)^m \right], \tag{5}$$

where *B*, *m*, and *n* are constants such that $n > m > 1$. The disjoining pressure, $-\Pi$, is negative for $h/h^* < 1$ and positive for $h/h^* > 1$, so that layer thickness is always forced toward the specified precursor film thickness. This effect becomes small for $h/h^* >> 1$. The disjoining pressure is related to a variety of additional forces that arise when two surfaces are brought in close contact with each other, the most prominent of which is van der Waals force. The constant *B* in (5) can be expressed in terms of the equilibrium contact angle $\theta_E$ as (Schwartz, 1998)

$$B = \frac{(n-1)(m-1)}{h^*(n-m)} \sigma(1 - \cos\theta_E). \tag{6}$$

A typical value for (*n*,*m*) is (3,2), although as shown by Schwartz and Eley (1998), the dynamics of the flow is not particularly sensitive to the values chosen for these coefficients.

We consider a constant flow rate condition in which the layer thickness approaches a constant value $h_\infty$ far upstream, which provides a characteristic length scale in the normal (*z*) direction. The characteristic length scale in the (*x*-*y*) plane tangent to the substrate is denoted by *L* and the characteristic time scale is denoted by *T*. We write the dimensionless precursor film thickness as $\delta \equiv h^* / h_\infty$ and the length-scale aspect ratio as $\varepsilon \equiv h_\infty / L$. Dimensionless variables are defined as

$$h' = h / h_\infty, \quad x' = x / L, \quad y' = y / L, \quad t' = t / T, \quad \Pi' = \Pi h_\infty / \sigma \delta^{m-1}. \qquad (7)$$

Substituting (4) - (7) into (3) and dropping the primes on the dimensionless variables, the dimensionless equation for liquid layer thickness becomes

$$\frac{\partial h}{\partial t} = -\nabla \cdot \left\{ P_1 [h^3 \nabla (\nabla^2 h) + \frac{\delta^{m-1}}{\varepsilon^2} h^3 \nabla \Pi] - P_2 h^3 \nabla h + h^3 \mathbf{e}_x \right\}. \qquad (8)$$

The parameters $P_1$ and $P_2$ are defined in terms of the tangential and normal Bond numbers, $Bo_T = h_\infty^2 \rho g_T / \sigma$ and $Bo_N = h_\infty^2 \rho g_N / \sigma$, as $P_1 = \varepsilon^3 / Bo_T$ and $P_2 = \varepsilon Bo_N / Bo_T$. The length scale *L* in the substrate tangent direction is set such that $P_1 = 1$, so that $\varepsilon = Bo_T^{1/3}$ and the normal body force parameter reduces to $P_2 = Bo_N / Bo_T^{2/3}$.

Nonlinear computations of liquid layer evolution are performed by solving (8) using a second-order ADI method for the lubrication equation. In some cases in which it is desirable to move the coordinates with the driven layer front, a convection term $Uh_x$ is added to the right-hand side of (7), where *U* is the front advection speed from the equilibrium theory. The computations are performed on a rectangular grid spanning the

interval $(x_{\min}, x_{\max})$ and $(y_{\min}, y_{\max})$ with uniform grid spacing. The boundary conditions are

$$h(x_{\min}, y) = 1, \quad h_x(x_{\min}, y) = 0, \quad h(x_{\max}, y) = \delta, \quad h_x(x_{\max}, y) = 0,$$
$$h_y(x, y_{\min}) = 0, \quad h_{yy}(x, y_{\min}) = 0, \quad h_y(x, y_{\max}) = 0, \quad h_{yy}(x, y_{\max}) = 0. \quad (9)$$

All computations reported in the report are performed for gravity-driven flow with tangential Bond number $Bo_T = \varepsilon^3 = 0.02$ and dimensionless precursor film thickness $\delta = 0.03$, unless otherwise indicated. The value of the Bond number only enters into the problem in the disjoining pressure term, and the results are not sensitive to small change in Bond number. The fingering instability is sensitive to variation in the precursor film thickness, with increase in the maximum instability growth rate as $\delta$ is decreased. The selection of $\delta$ depends on the specific experimental conditions under consideration. Kataoka and Troian (1997) report good comparison between several different experimental studies and computations for fingering stability in shear-driven flow with $\delta = 0.01$. Values of $\delta$ in the range 0.01-0.03 have been used by numerous investigators and have consistently yielded results in at least qualitative (and often quantitative) agreement with experiments.

B. Equilibrium Profile and Linear Stability

One limiting consideration is that resolution of the flow field requires the grid spacing $\Delta x$ to be on the order of or smaller than the precursor film thickness. This restriction is necessary due to a small undershoot in the liquid layer thickness close to the contact point. This undershoot is shown in Figure 17b, which gives a close-up view of the region indicated by a dashed circle in Figure 17a. The length of this undershoot region is proportional to the precursor film thickness (with a typical length of about $6\delta$), such that the smaller the precursor film thickness the smaller the grid spacing necessary to resolve this region. We note that the magnitude of the disjoining pressure (which we use to introduce the effect of contact angle variation) is greatest in this undershoot region near

the contact line, and for this reason we take care in the current study to ensure that this undershoot region is well resolved.

An equilibrium solution $h_0(x-Ut)$ for liquid layer thickness is obtained from (7) using the convected coordinate $\xi \equiv x-Ut$, where the equilibrium front advection speed is obtained as $U=(1-\delta^3)/(1-\delta)$. Results for the equilibrium layer thickness in gravity-driven flow are shown in Figure 18a for cases with different values of the normal force parameter $P_2$ and in Figure 18b for different values of the static contact angle $\theta_E$. For $P_2=0$ and no disjoining pressure (upper solid curve in Figure 18a), there exists a "ridge" in the liquid layer thickness just before the front measuring 47% of the upstream liquid layer thickness. As $P_2$ increases, the thickness of the liquid ridge gradually decreases. Increase in contact angle has the opposite effect to that of the normal gravity. When the contact angle is increased slightly to $\theta_E=0.1$ (radians), with zero normal body force, the ridge thickness is nearly unchanged. (The solid curve in Figure 18b is both the cases for $\theta_E=0$ and $\theta_E=0.1$ plotted on top of each other.) However, if the contact angle is increased more substantially, such as to $\theta_E=0.3$ (dashed curve), the ridge exhibits a slight increase in maximum thickness to about 55% of the upstream liquid layer thickness.

Stability of the equilibrium solution is examined for perturbations that are periodic in the spanwise ($y$) direction, such that the layer thickness is given by

$$h(x,y,t)=h_0(\xi)+G(\xi,t)\exp(iky), \tag{10}$$

where $k$ is the spanwise perturbation wavenumber. Substituting (10) into (8) and linearizing gives a fourth-order differential equation for the perturbation amplitude $G(\xi,t)$, which is subject to the boundary condition that the perturbations die away far upstream and far downstream of the front, or $G, G_\xi \to 0$ as $\xi \to \pm\infty$. This equation is solved numerically for $G(\xi,t)$ using a second-order Crank-Nicholson method similar to

that employed for solving for the equilibrium layer profile $h_0(\xi)$. After the initial transient dies away, the computed perturbation amplitude is found to approach a separable form $G(\xi,t) \to A(\xi)e^{\beta t}$, where $A(\xi)$ specifies the spatial form of the eigenfunction and $\beta$ is the growth rate corresponding to perturbations with spanwise wavenumber *k*. In the reported linear stability computations, we set the computational domain as (-50,5), with the front occurring at $x = 0$, and the space and time step as $\Delta x = 0.0069$ and $\Delta t = 0.005$. Tests with smaller values of $\Delta x$, $\Delta t$, and $x_{\min}$ indicate that the uncertainty in the instability growth rates reported in the paper is less than 2%, with the greatest sensitivity due to variation in $\Delta x$. These same tests indicate uncertainty in the maximum equilibrium layer thickness to be less than 0.4%.

The computed growth rate is plotted in Figure 19a as a function of wavenumber for cases with precursor film thickness of 0.03 and 0.1 with no disjoining pressure or normal body force. Data from the stability calculations of Bertozzi and Brenner[8] with $\delta = 0.1$ are denoted by circles in Figure 19a and are found to compare well with the current computations. For $\delta = 0.03$, the liquid layer front is unstable for dimensionless wavenumbers below a critical value of $k_{crit} = 0.7$, with the most unstable waves corresponding to a wavenumber of about $k_{\max} = 0.47$. Growth rate for cases with different values of $P_2$ are shown in Figure 19b with disjoining pressure set to zero. As noted by Bertozzi and Brenner[8], increase in the normal force parameter $P_2$ decreases both the growth rate and the maximum wavenumber of the fingering instability. When $P_2$ increases above a critical value $P_{2,crit}$, the front is linearly stable for all wavenumbers. The growth rate is not significantly altered by a small change in contact angle, as was also observed by Spaid and Homsy (1996) using a local slip model to treat the contact line singularity. The above trends in growth rate are supportive of the idea that the front becomes more susceptible to fingering instability as the liquid ridge thickness in the equilibrium solution increases and less susceptible as the ridge thickness decreases.

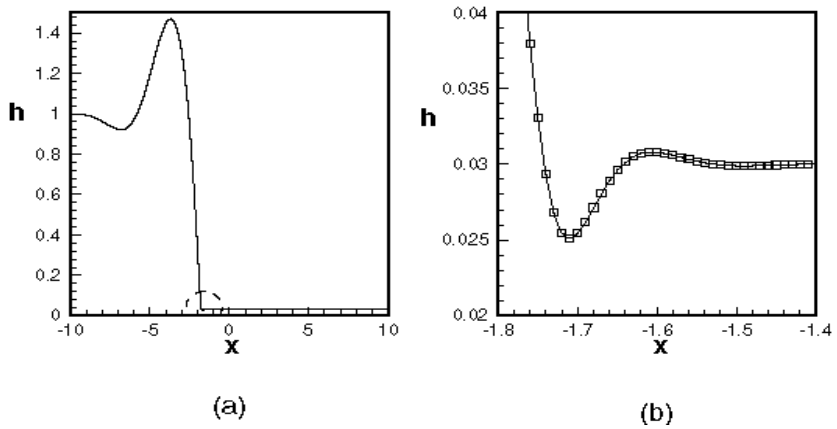


Figure 17. Plots of (a) equilibrium layer thickness profile versus position along the substrate and (b) a close-up showing the overshoot in layer thickness in the region indicated by a dashed half-circle in (a). The symbols in (b) are the numerical computation points.

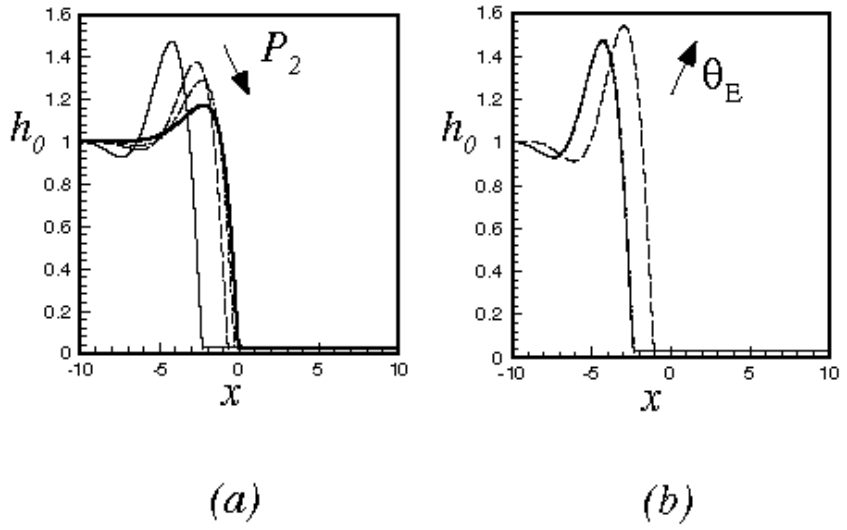


Figure 18. Variation of equilibrium layer profiles with (a) normal body force and (b) contact angle. Figure (a) shows cases with $P_2 = 0$ (upper solid curve), 0.5 (dashed curve), 1.0 (dashed-dotted curve) and 2.0 (lower heavy solid curve). Figure (b) shows cases with $\theta_E = 0$ (lower solid curve), 0.1 (dashed-dotted curve, coincident with the $\theta_E = 0$ case), and 0.3 (dashed-dotted curve).

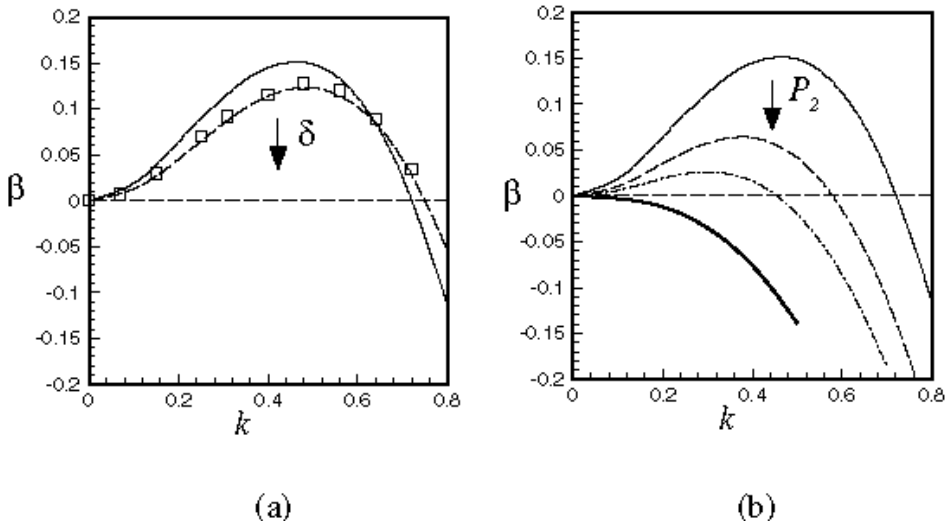


Figure 19. Instability growth rate as a function of wavenumber for cases with (a) different values of precursor film thickness $\delta$ (with $P_2 = 0$) and (b) different values of the normal body force parameter $P_2$ (with $\delta = 0.03$). Figure (a) shows computational results for $\delta = 0.03$ (solid curve) and for $\delta = 0.1$ (dashed curve), as well as comparison data from Bertozzi and Brenner (1997) for $\delta = 0.1$ (symbols). Figure (b) shows cases with the same values of $P_2$ as in Figure 18.

C. Validation of Predictions for Dynamic Contact Angle

Despite its usage in several papers in the literature, the disjoining pressure expression (5) with the coefficient (6) has never been thoroughly validated. In particular, there is no demonstration in the literature that by introducing this disjoining pressure term the computed dynamic contact angle is correct. We have examined this question by performing a series of two-dimensional computations with different values of the static contact angle $\theta_E$, the tangential Biot number $Bo_T$, and the precursor film thickness $\delta$. The computed contact angle in these computations is determined by fitting a straight line to the part of the film thickness curve with greatest slope near the region where the film meets the precursor film. The computed results for dynamic contact angle are compared to the Tanner-Hoffman-Voinov formula (Tanner, 1979; Hoffman, 1975; Voinov, 1976), given by

$$\theta^3 = \theta_E^3 + D\mu U / \sigma\,, \tag{11}$$

where $D$ is a constant and $U$ is the contact line velocity. Defining dimensionless contact angles by $\theta' \equiv \theta / \varepsilon$ and using the scaling (7) with $\varepsilon^3 = Bo_T$ and the equilibrium solution for $U$, we can rewrite (11) in the dimensionless form

$$\theta'^3 = C[\theta_E'^3 + A(1-\delta^3)/(1-\delta)]\,, \tag{12}$$

where $A$ is a constant and $C = 1$ for the Tanner-Hoffman-Voinov formula.

It is found in all cases examined that the cube of the computed dynamic contact angle $\theta'^3$ varies nearly linearly with the cube of the static contact angle $\theta_E'^3$. Several examples of this linear relationship are shown in Figure 20 for different values of the precursor film thickness and for Biot numbers of $Bo_T = 0.02$ and 0.002. The slope of the best-fit linear relationship is determined by data regression and plotted in Figure 21a. The predicted slopes for the two different Biot number cases are nearly identical. It is observed that the slope deviates significantly from the unit value (given by Eqn. (12)) for finite precursor film thicknesses, but seems to approach unity as $\delta \to 0$. The uncertainty in this data is estimated by the variation in the best-fit line from the data. The relative error in dynamic contact angle is approximately $1 - C^{1/3}$, which is plotted as a function of $\delta$ in Figure 21b. These results indicate that the disjoining pressure expression (5)-(6) yields reasonable quantitative agreement with the classical Tanner-Hoffman-Voinov dynamic contact angle formula for $\delta \le 0.01$ (with relative error in contact angle less than 5%), and that it might yield reasonable qualitative agreement with this formula for $\delta \le 0.05$ (with relative error in contact angle less than 20%). It is noted that this comparison is still preliminary, and that we are currently performing a detailed grid dependence test for small values of $\delta$, which exhibit unusually high data uncertainty.

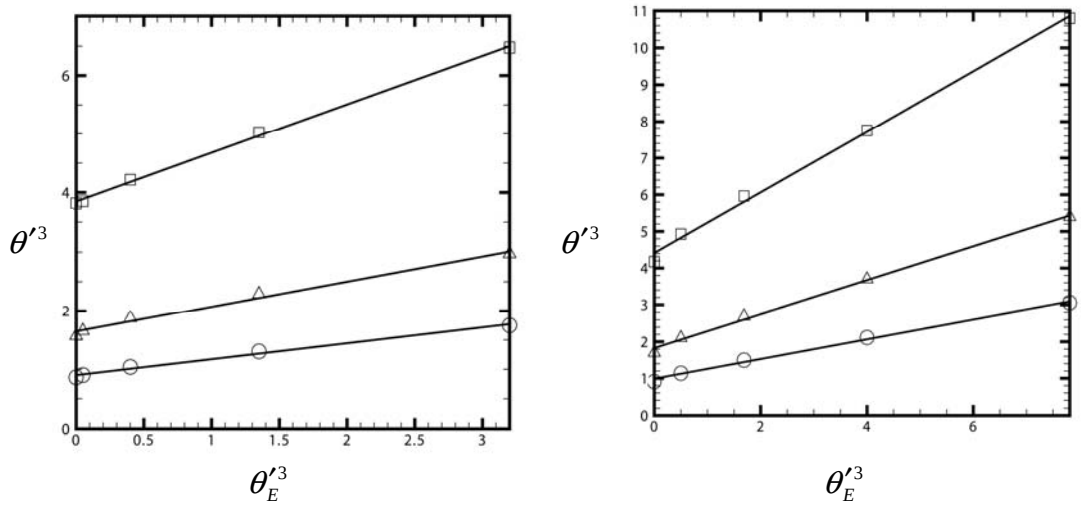


Figure 20. Plots showing cube of dynamic contact angle versus cube of static contact angle for cases with precursor film thickness $\delta = 0.01$ (squares), 0.05 (triangles) and, 0.1 (circles) for (a) $Bo_T = 0.002$ and (b) $Bo_T = 0.02$.

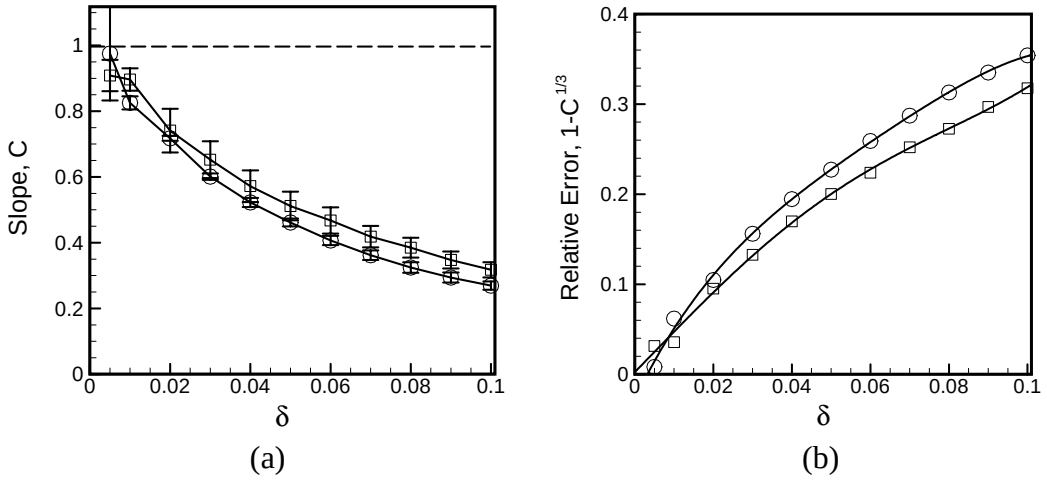


Figure 21. Plots showing (a) slope $C$ from Eqn. (12) and (b) relative error estimate $(1-C)^{1/3}$ in dynamic contact angle for $Bo_T = 0.02$ (circles) and $Bo_T = 0.002$ (squares) as a function of precursor film thickness $\delta$.

D. Results for a Single Contamination Spot

Computations were performed for driven liquid film front passed an isolated contamination spot, having static contact angles either greater than and or less than the ambient contact angle. The contamination spot is modeled by a Gaussian variation in contact angle centered at a point $(x_D, y_D)$, with a Gaussian decay radius *R* and maximum difference $\Delta\theta_{E,\max}$ in contact angle compared to the ambient value $\theta_E$. All computations reported in this section are performed with an ambient contact angle $\theta_E = 0.1$ and precursor film thickness $\delta = 0.03$.

As noted by Greenspan (1978) in his theoretical study of droplet behavior in regions with variable contact angle, the liquid within the layer is drawn toward regions of small static contact angle and repelled from regions with larger static contact angle. The important parameter in determining the liquid layer behavior is not the contact angle itself, but the gradient in contact angle. Thus, even though the form and dynamics of the front is nearly identical for the case with a uniform static contact angle $\theta_E = 0.1$ and that with no disjoining pressure ($\theta_E = 0$), a slight spatial variation in static contact angle can have a large effect on the front. For instance, a time series showing impact of a liquid layer front on spot with a decrease in static contact angle spots, $\Delta\theta_{E,\max} = -0.01$, is shown in Figure 22. As the front passes through the spot with negative relative contact angle spot, liquid from the surrounding regions of the front is attracted toward by the spot, forming a slight bulge in the thickness of the liquid film ridge just downstream of the spot and regions of decreased layer thickness on either side of this bulge. The opposite occurs for a spot with a positive relative contact angle. Since the front itself is unstable, these disturbances grow with time with a length scale on the order of the fastest-growing wave from linear stability theory, which is indicated by an arrow in Figure 22c. A plot showing the change in the maximum layer thickness $\Delta h_{\max}$ versus time is given in Figure 22d. After the initial transient, the growth rate of the layer thickness is nearly the same as that of the fastest-growing wavelength from linear theory (indicated by a dashed line in Figure 22d).

The effect of contact angle variation $\Delta\theta_{E,\max}$ within the spot on the instability growth rate is examined in Figure 23. Cases with positive relative contact angle spots are plotted in Figure 23a, for $\Delta\theta_{E,\max} = 0.01$, 0.02 and 0.05, and cases with negative relative contact angle spots are plotted in Figure 24b, with $\Delta\theta_{E,\max} = -0.01$, –0.02, and –0.05. As might be expected, cases with higher value of $\Delta\theta_{E,\max}$ exhibit greater initial layer thickness increase, but then all cases exhibit about the same growth rate after the initial transients have died away. It is not until the change in maximum layer thickness exceeds about 50% of the ambient layer thickness that the growth in thickness of the film becomes saturated by nonlinear effects and the layer thickness approaches a constant value. Computations were performed with values of the ambient contact angle $\theta_E$ of 0.1, 0.2 and 0.3, but the same value of the contact angle change $\Delta\theta_{E,\max}$ within the spot. The results in all three cases are nearly identical, demonstrating that it is not the ambient contact angle that matters to the fingering phenomenon, but rather the variation in contact angle.

The effect of contamination spot radius on the front instability is illustrated in Figure 24 for cases with $R = 0.5$, 1.0 and 5.0. The three contour plots in Figure 24a-c and the profiles of $h_{\max}$ versus spanwise distance *y* in Figure 24d are all drawn at the same time. All three cases exhibit growth in the layer thickness with about the same spanwise length scale. The layer perturbation amplitude is much smaller for the case with $R = 0.5$ than for the other two cases, whereas the maximum layer thickness is about the same for the cases with $R = 2$ and $R = 5$.

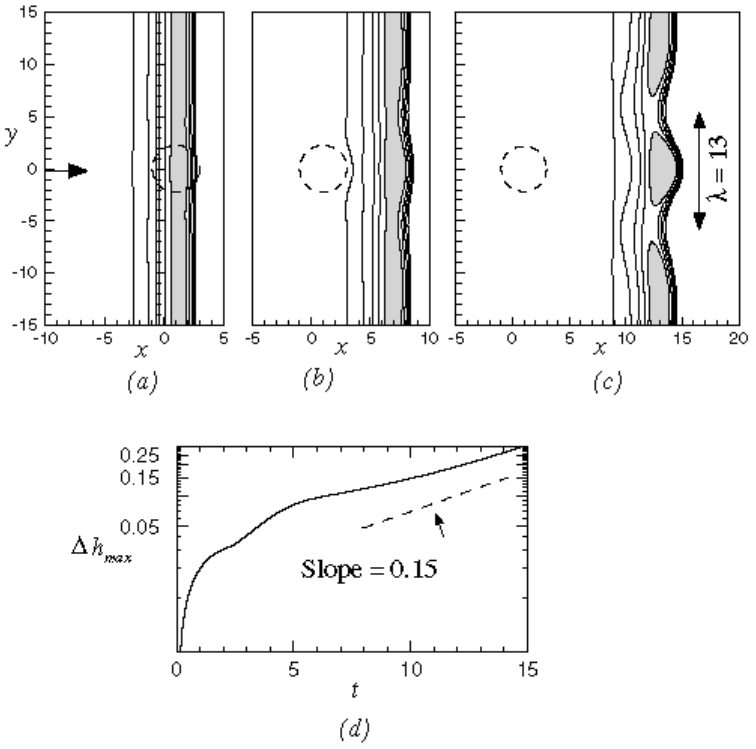


Figure 22. Contours of layer thickness for contact line motion past a contamination spot with negative relative contact angle at times (a) $t = 5$, (b) 10, and (c) 15. The dashed line in (d) indicates the growth rate prediction from the linear stability theory.

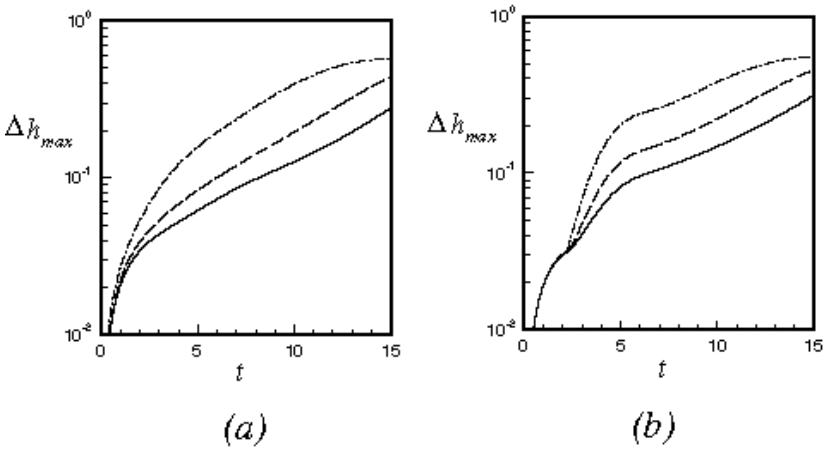


Figure 23. Effect of maximum contact angle variation $\Delta\theta_{E,\max}$ on time variation of the change in maximum layer thickness for cases with (a) positive relative contact angle and (b) negative relative contact angle. Cases are shown with $\Delta\theta_{E,\max} = \pm 0.1$ (solid curve), $\pm 0.2$ (dashed curve), and $\pm 0.5$ (dashed-dotted curve).

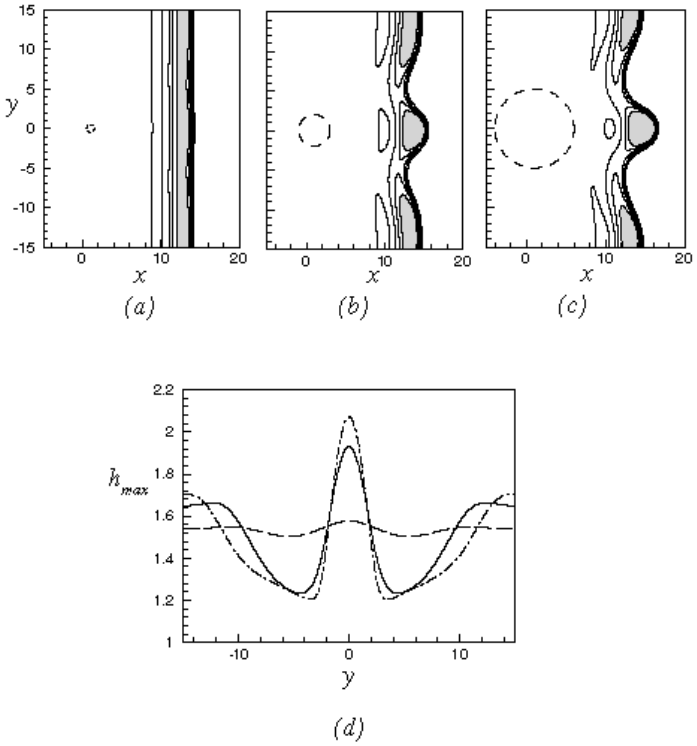


Figure 24. Contours of layer thickness showing effect of contamination spot radius on the liquid layer at time $t = 15$ for cases with (a) $R = 0.5$, (b) 2.0, and (c) 5.0. The profile of the maximum value of layer thickness is plotted versus *y* at the same time in Figure (d) for $R = 0.5$ (dashed curve), 2.0 (solid curve) and 5.0 (dashed-dotted curve).

E. Results for an Array of Contamination Spots

We now examine the nonlinear behavior of the liquid layer front when it passes through an ordered array of contamination spots. We particularly focus on nonlinear features of the fingering instability in the presence of multiple impacts on contamination spots, including behavior such as layer thickness saturation, wavenumber selection, and sub-critical instability. For all cases examined in this section, the background contact angle is $\theta_E = 0.1$, the spot radius is $R = 2$, and the precursor film thickness is $\delta = 0.05$. A slightly larger precursor film thickness is used than in the previous section in order to allow us to use a slightly larger grid increment ($\Delta x = \Delta y = 0.015$) while still fully resolving the flow near the contact line. Sample computations with $\delta = 0.03$ exhibit no significant differences with the present results.

Time series showing contours of the layer thickness for a $4\times4$ spot array with spot spacing distance $\lambda=10$ is given in Figure 25 for $\Delta\theta_{E,\max}=0.05$ and in Figure 26 for $\Delta\theta_{E,\max}=-0.05$. The spots are indicated by dashed circles in these figures, and the region with largest layer thickness is shaded gray. The spot spacing distance used for these computations corresponds to a wavelength $k=0.63$, for which the liquid layer front is unstable. For spots in which the contact angle increases, the rivulets form in the interstitial region between the spots, whereas for spots with a decrease in contact angle rivulets protrude from the region of the front that passes through the spot. The maximum layer thickness increases rapidly as the front impacts on the first row of spots and continues to grow up to a time of about $t=10$, at which point the front is just impacting the second row of spots. Beyond this time, the maximum layer thickness saturates at a value of about 1.5 times its initial value, where the thickest part of the rivulet occurs in a droplet at the rivulet tip and along the ridge at the rivulet center. This maximum thickness value oscillates somewhat, but does not increase in the mean with later time. As might be expected, the oscillation amplitude is larger for cases where $\Delta\theta_{E,\max}>0$, where the rivulets impact directly on the spots, than for cases with $\Delta\theta_{E,\max}<0$, where the rivulets pass in-between the spots. The rivulet length progressively increases throughout the computation.

In Figure 27 we show results for two cases where the spot spacing distance $\lambda$ is smaller than the critical value for the fingering instability, such that the front is stable to linear perturbations at the forcing wavenumber specified by the spot spacing. In Figure 27a, the spot spacing $\lambda=7.5$ is slightly below the critical value $\lambda_{crit}=9.4$. Nevertheless, the liquid layer front is observed to break up into thin rivulets that thread in-between the spots with width equal to $\lambda$. This result indicates that substrate surface contamination can lead to rivulet development even for wavelengths for which the front is stable to linear fingering instability. The plot of change in maximum layer thickness versus time in Figure 27c again exhibits saturation of the liquid layer thickness at about 1.5 times its initial value.

On the other hand, when the spot spacing is too small, the perturbations induced by the spots will be suppressed, such that the fastest growing wave of the linear stability theory will dominate. Such a case is exhibited in Figure 27b, where the spot separation distance $\lambda = 5$ is so small in comparison to the critical wavelength that rivulets will not form on this small scale. Instead, we observe formation of a large central rivulet (with width of about 15) and a smaller rivulet (width ≈ 8) on either side. Both the central rivulet and the side rivulets pass directly over the positive relative contact-angle contamination spots. The plot of maximum layer thickness for this case, shown in Figure 27c, exhibits a progressive increase with time with oscillations occurring when the front tip passes over a contamination spot. We therefore observe that a sub-critical instability will dominate for spot separation distance in some interval $\lambda_{sub} < \lambda < \lambda_{crit}$ below the critical wavelength $\lambda_{crit}$ obtained from linear stability theory, where the value of $\lambda_{sub}$ is dependent on $\Delta\theta_{E,\max}$. Interactions with values of $\lambda$ much smaller than $\lambda_{sub}$ can lead to hysteresis of the front advection speed (as examined by Schwartz[22]), but not to development of rivulets.

The effect of normal body force on rivulet development is illustrated in contour plots of layer thickness in Figure 28 and 29 for $P_2 = 1$ and 2, respectively, and $\lambda = 10$. Both of these cases are stable according to the linear stability theory. The change in maximum liquid film thickness is plots as a function of time for three cases (with $P_2 = 0$, 1 and 2) in Figure 30. In the case with $P_2 = 1$, protrusions of the liquid layer front gradually develop in-between the spots. The maximum layer thickness oscillates around a mean value of about 1.2 times its initial value. During the course of the current computations the protrusion length continued to increase in time, although more slowly than with no normal body force. For the $P_2 = 2$ case (for which the liquid layer front is linearly stable for all perturbation wavenumbers), the front develops a slight wavy appearance as it passes through the contamination spot array. The maximum layer thickness for this case oscillates with a mean value of only about 1.07 times its initial value. Comparison of Figure 29b and 29c suggests that the shape of the liquid layer front returns to approximately the same form as each set of spots is passed, without significant change in

layer thickness or protrusion length. This behavior is characteristic of a case in which rivulet formation has been suppressed by sufficiently large normal body force.

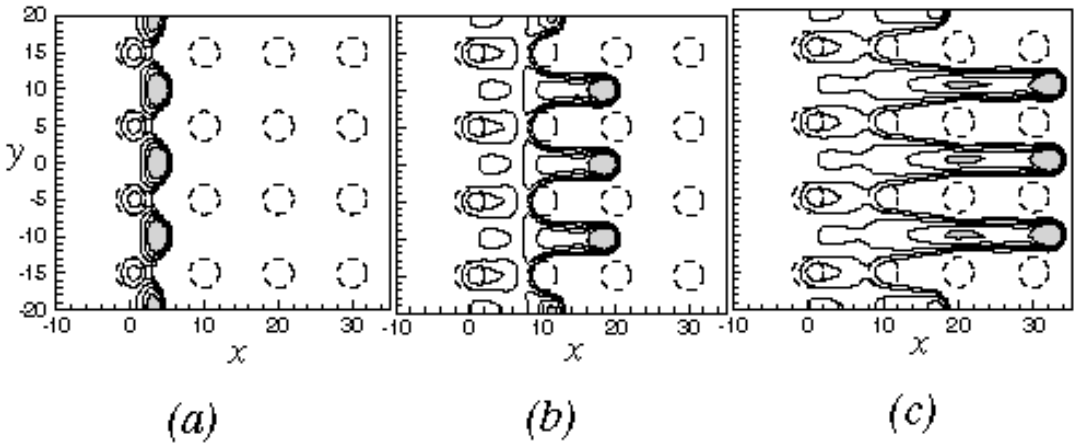


Figure 25. Contour plots of the layer thickness showing rivulet development for passage of a driven front through a symmetric array of positive relative contact angle spots, at times (a) $t = 5$, (b) $t = 15$, and (c) $t = 24$.

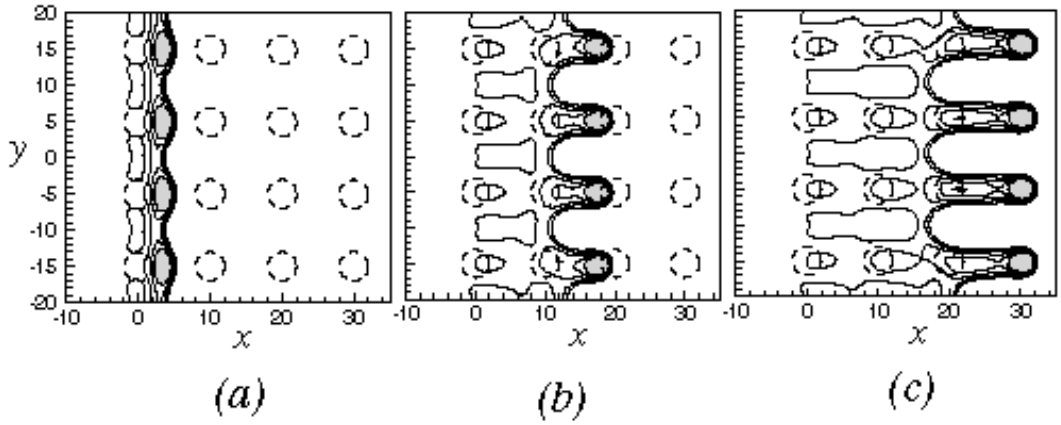


Figure 26. Contour plots of the layer thickness showing rivulet development for passage of a driven front through a symmetric array of negative relative contact angle spots, at times (a) $t = 5$, (b) $t = 15$, and (c) $t = 24$.

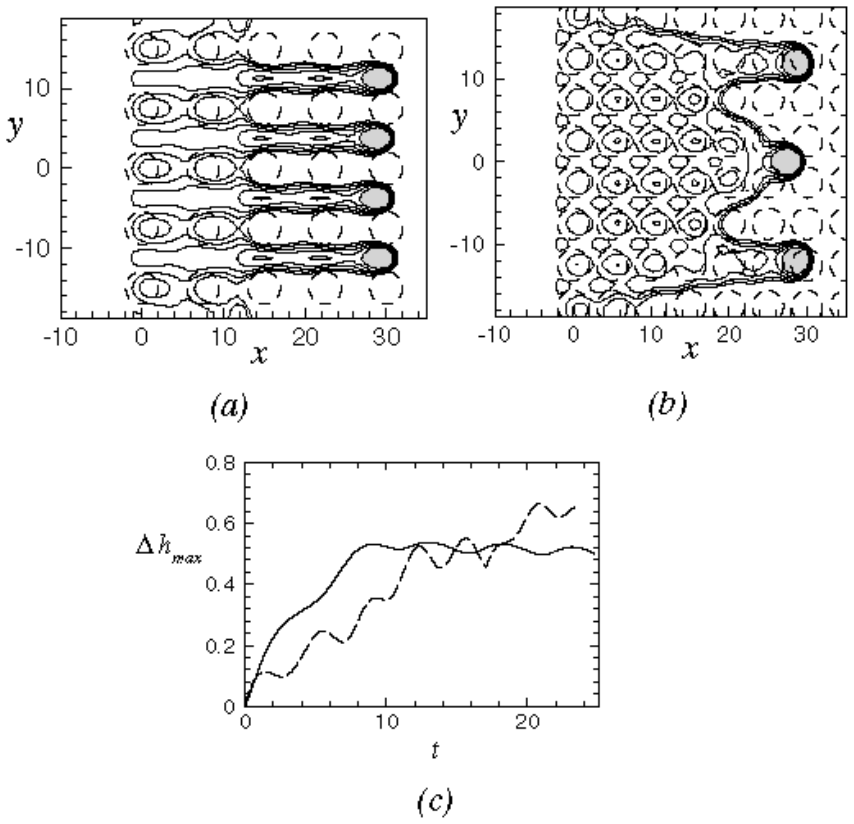


Figure 27. Plots illustrating passage of a driven layer front through a symmetric array of positive relative contact angle spots with spacing $\lambda$ less than the critical value for instability: (a) case with $\lambda = 7.5$ showing sub-critical instability induced by contamination spots, (b) case with $\lambda = 5$ showing rivulet develop with spacing greater than $\lambda$, (c) time variation of change in maximum layer thickness for (a) (solid curve) and (b) (dashed curve).

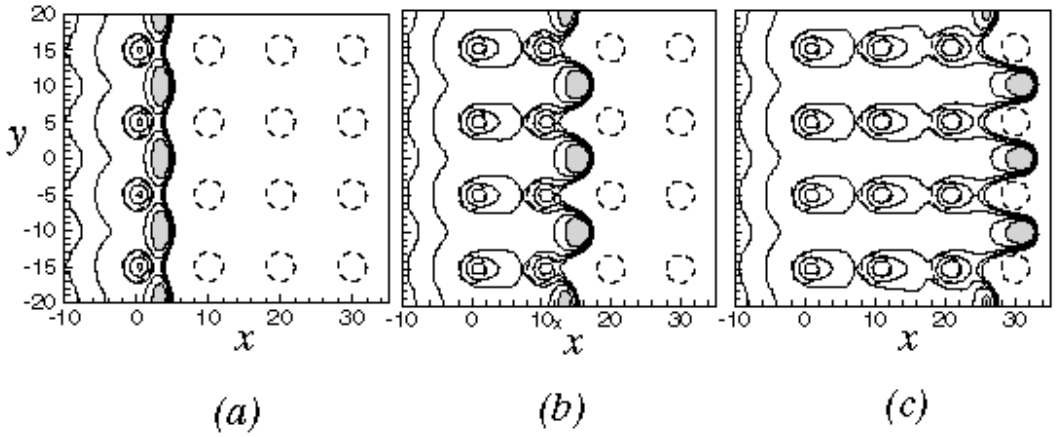


Figure. 28. Time series showing contour lines of layer thickness for a case with $P_2 = 1$ and a symmetric array of positive relative contact angle spots, at times (a) $t = 5$, (b) $t = 15$, and (c) $t = 25$. Five evenly spaced contours are plotted over the interval $(0.8,1.2)$, and gray shading indicates regions where $h > 1.2$.

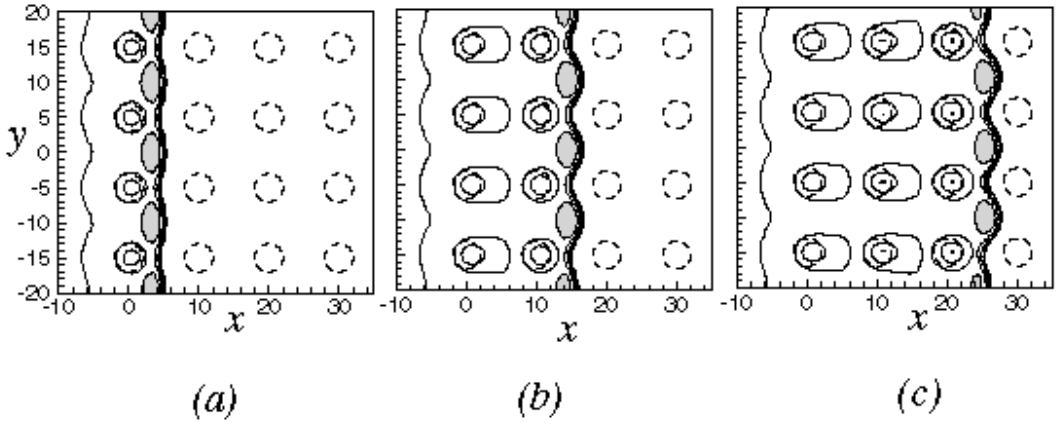


Figure. 29. Time series showing contour lines of layer thickness for a case with $P_2 = 2$ and a symmetric array of positive relative contact angle spots, at times (a) $t = 5$, (b) $t = 15$, and (c) $t = 25$. Five evenly spaced contours are plotted over the interval $(0.7,1.1)$, and gray shading indicates regions where $h > 1.1$.

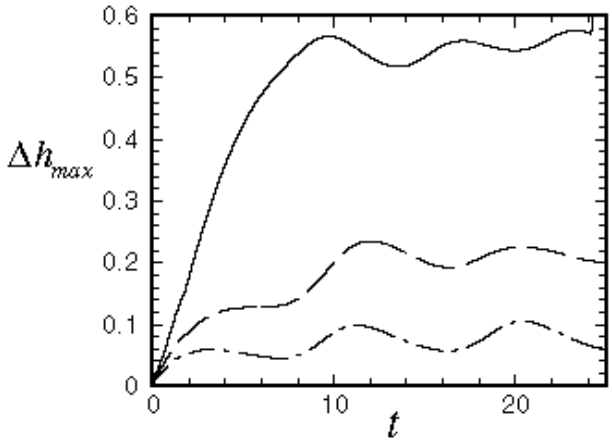


Figure 30. Effect of $P_2$ on time variation of the change in maximum layer thickness for cases with $P_2 = 0$ (solid curve), $P_2 = 1$ (dashed curve), and $P_2 = 2$ (dashed-dotted curve).

F. Results for Surfaces with Random Contact Angle Variation

For natural surfaces, contamination and roughness variation occur not in ordered arrays, but rather in a random manner. Nevertheless, even on a random surface one can characterize the variation of a function on the surface in terms of one of more dominant

length scales and a variance of the function about a mean value. To examine the effect of surface inhomogeneity on contact line stability and fingering for more natural surfaces, we implemented a method developed by Hu and Tonder (1992) for generation of a random surface with an autocorrelation function given by

$$R(k,m) = \gamma^2 \exp[-2.3\{(k/\ell_x)^2 + (m/\ell_y)^2\}], \qquad (13)$$

where $\gamma$ is the variance, $k$ and $m$ are the wavenumbers in the $x$ and $y$ directions, and $\ell_x$ and $\ell_y$ are the correlation lengths in the $x$ and $y$ directions. The correlation lengths are defined as the lengths at which the autocorrelation function of the $x$ and $y$ profiles reduce to 10% of there values at the origin.

Samples of random surfaces generated with correlation lengths of 4 and 16 are shown in Figure 31. The fastest-growing length scale of the linear stability theory for this case is about 15. A time series showing the film thickness contours at times $t = 15$, 30, and 60 for these two values of the correlation length are shown in Figure 32. Both cases exhibit finger growth, but the average spacing between fingers is somewhat less for the case with lower correlation length ($\lambda \cong 18$) than for the case with larger correlation length ($\lambda \cong 23$). We also observe significant variation in finger spacing between adjacent fingers for both of these cases with random static contact angle variation.

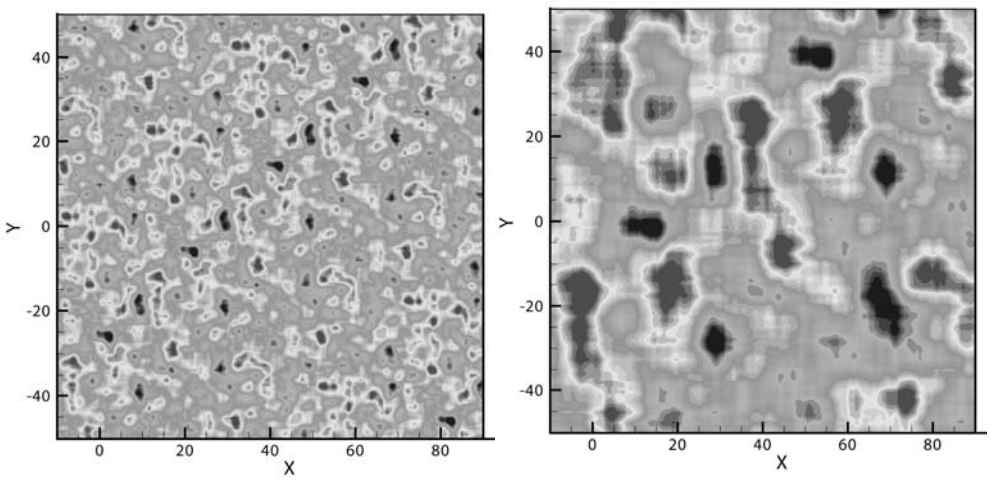


(a) (b)

Figure 31. Random surfaces generated using correlation lengths (a) $\ell_x = \ell_y = 4$ and (b) $\ell_x = \ell_y = 16$.

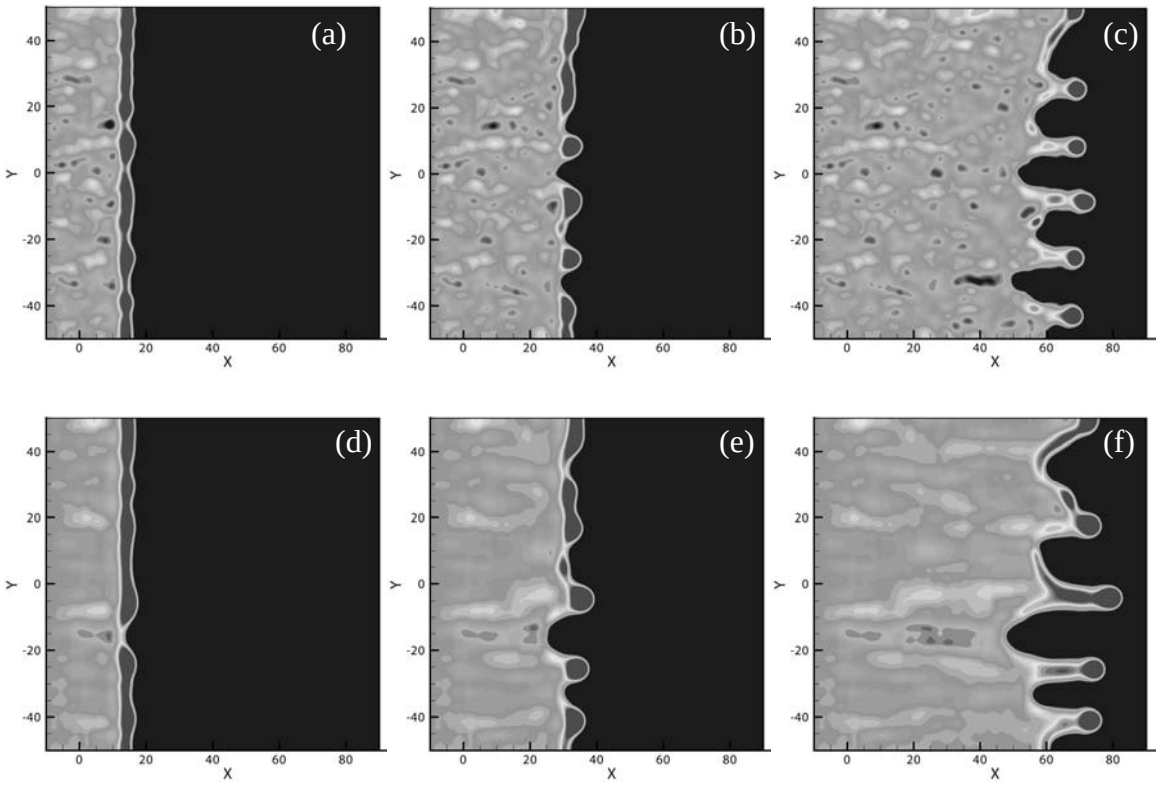


Figure 32. Results for finger growth on a driven liquid film over a surface with contact angle variation with correlation length $\ell = 4$ (a-c) at times $t = 15$, 30, and 60, and with correlation length $t = 16$ (d-f) at the same three times.

## III. References Cited


Bertozzi, A.L. and Brenner, M.P., "Linear stability and transient growth in driven contact lines," *Physics of Fluids* **9**(3), 530-539 (1997).

de Gennes, P.G., "Wetting: statics and dynamics," *Reviews of Modern Physics* 57(3), 827-863 (1985).

Greenspan, H.P., "On the motion of a small viscous droplet that wets a surface," *Journal of Fluid Mechanics* 84, 125-143 (1978).

Hoffman, R.L., "A study of the advancing interface. Part 1. Interface shape in liquid-gas systems," *Journal of Colloid and Interface Science* **50**(2), 228-241 (1975).

Hu, Y.Z. and Tonder, K., "Simulation of 3-D random rough surface by 2-D digital filter and Fourier analysis," *International Journal of Machine Tools and Manufacturing* **32**(1/2), 83-90 (1992).

Kataoka, D.E. and Troian, S.M., "A theoretical study of instabilities at the advancing front of thermally driven coating layers," *J. Colloid Interface Sci.* **192**, 350-362 (1997).

Schwartz, L.W., "Hysteric effects in droplet motions on heterogeneous substrates: Direct numerical simulation," *Langmuir* **14**, 3440-3453 (1998).

Schwartz, L.W. and Eley, R.R., "Simulation of droplet motion on low-energy and heterogeneous surfaces," *J. Colloid Interface Sci.* **202**, 173-188 (1998).

Spaid, M.A. and Homsy, G.M., "Stability of Newtonian and viscoelastic dynamic contact lines," *Physics of Fluids* **8**(2), 460-477 (1996).

Tanner, L.H., "The spreading of silicone oil drops on horizontal surfaces," *Journal of Physics D: Applied Physics* **12**, 1473-1484 (1973).

Voinov, O.V., "Hydrodynamics of wetting," *Izvestiya Akademii Nauk SSSR, Mekhanika Zhidkosti I Gaza*, No. 5, pp. 76-81 (1976).


## IV. List of Students Supported by the Project

Yongli Zhao (Ph.D. student), started program August 2002. Working on computational modeling of thin film stability on heterogeneous contaminated surfaces, and computation of films with finite inertia. Expected graduation August 2005.

John Mousel (B.S./M.S. joint degree program student), started working August 2003 as an undergraduate research assistant. Working on experimental study of wind-driven droplet dynamics. Expected graduation May 2006.

Geoff McAlister, graduated August 2003 with an M.S. in Mechanical Engineering. Worked on microgravity and terrestrial gravity experiments of rivulet breakup.

Shufang Wang, graduated August 2002 with an M.S. in Mechanical Engineering. Worked on computational modeling of thin film motion past contamination spots and droplets.

## V. List of Papers and Theses

A. Journals / Review Articles

McAlister, G., Ettema, R. and Marshall, J.S., "Wind-driven rivulet break-off and droplet flows in microgravity and terrestrial gravity conditions," *Journal of Fluids Engineering*, 2004 (in press).

Marshall, J.S. and Ettema, R., "Contact-line instabilities of driven liquid films," *Advances in Fluid Mechanics* (*Instability of Flows*, edited by M. Rahman), WIT Press, Southampton, England, 2004 (in press).

Marshall, J.S. and Wang, S., "Contact-line fingering and rivulet formation in the presence of surface contamination," *Computers and Fluids*, 2004 (in press).

Zhao, Y. and Marshall, J.S., "Dynamics of driven liquid films over heterogeneous surfaces," in preparation.

B. Theses

McAlister, G., "The breakup of sheet flow to rivulets and rivulets to droplets," M.S. Thesis, University of Iowa, Iowa City (2003).

Wang, S., "Contact-line receptivity and rivulet initiation in the presence of droplets and surface contamination," M.S. Thesis, University of Iowa, Iowa City (2002).

C. Conferences

Ettema, R., Marshall, J.S. and McAlister, G., "Wind-driven rivulet break-off in conditions ranging from 0g to 1g," Workshop on Strategic Research to Enable NASA's Exploration Missions, Cleveland, Ohio, June 22-23 (2004) (poster and abstract).

Wang, S. and Marshall, J.S., "Effect of normal body force on fingering instability of a liquid sheet driven by shear stress or gravity," Joint ASME-European Fluids Engineering Summer Conference, Montreal, July 14-18 (2002).

Wang, S., McAlister, G., Marshall, J.S. and Ettema, R., “Rivulet dynamics with variable gravity and wind shear,” Fifth Microgravity Fluid Physics and Transport Phenomena Conference, Cleveland, Ohio, August 13-16 (2002) (poster and abstract).